The phonon dispersion and lattice dynamics of alpha -$AlPO_4$: an inelastic neutron scattering study

1992 J. Phys.: Condens. Matter 4 5537

(http://iopscience.iop.org/0953-8984/4/25/007)

J. Phys.: Condens. Matter 4 (1992) 5537–5550. Printed in the UK

The phonon dispersion and lattice dynamics of α-$AlPO_4$: an inelastic neutron scattering study

J Bethke†‡, G Eckold†‡ and Th Hahn†

† Institut für Kristallographie, RWTH Aachen, D-5100 Aachen, Federal Republic of Germany

‡ Institut für Festkörperforschung, KFA Jülich, POB 1913, D-5170 Jülich, Federal Republic of Germany

Received 23 December 1991, in final form 3 April 1992

Abstract. The low-energy part of the phonon dispersion of the quartz isotype α-$AlPO_4$ has been investigated by inelastic neutron scattering. The experimental data are reproduced by different lattice dynamical models. Good quantitative agreement with experimental neutron, Raman and infrared data is achieved even with just a simple five-parameter Born–von Karman model. The results are compared with the lattice dynamics of quartz. As a main result, it is found that the lattice dynamics at low frequencies is essentially determined by the properties of the oxygen framework, irrespective of the specific nature of the central atoms within the oxygen tetrahedra. The dynamical stability of the lattice is discussed with regard to the incommensurate phase transition.

1. Introduction

For a long time, the phase transition of the quartz structure from the low (α-) phase to the high (β-) phase has been regarded as the prototype of a displacive phase transition. The detection of the incommensurate phase, however, has brought into question the simple transformation mechanism based on a single optical Γ-point soft mode. Careful inelastic neutron scattering investigations on SiO_2 revealed that it is in fact not a *single* phonon but the anharmonic coupling between *several* phonon modes that triggers this phase transition [1]. Thus, new light was shed on the α–β phase transition and a more detailed microscopic model could be obtained.

Among the isotypes of quartz, there are some ternary compounds such as $AlAsO_4$, $GaAsO_4$, $GaPO_4$ in which this phase transition is suppressed. On the other hand, $AlPO_4$ (Berlinite), $FePO_4$, BeF_2 and GeO_2 exhibit both the low-phase and the high-phase quartz structure. Interestingly, in spite of the different natures of the constituents in $AlPO_4$ not only is the transition temperature ($T \simeq 857$ K) very close to that of quartz, but also an incommensurate phase very similar to that found in SiO_2 has been detected [2]. Therefore, $AlPO_4$ is a good candidate on which to test the influence of different types of atoms on the phase transition. Furthermore, this compound has aroused considerable technical interest within the last few years as a possible substitute for quartz, since it provides an improved thermal performance as a resonator; cf [3]. In contrast to other quartz isotypes, single crystals of $AlPO_4$ are available that exhibit high optical quality and sufficiently large volumes. Hence, this

0953-8984/92/255537+14$04.50

compound is particularly suitable as a subject for a detailed investigation of dynamical behaviour using inelastic neutron scattering.

In this paper, the first of a series, we present the low-frequency part of the phonon dispersion of α-$AlPO_4$ at room temperature along with a simple lattice dynamical model. Subsequent papers will deal with the temperature dependence of selected phonons, with the properties near the phase transition and with dynamical features of the incommensurate phase.

2. Symmetry restrictions

The $AlPO_4$ (Berlinite) structure consists of a three-dimensional network of nearly regular corner-linked tetrahedra as in the quartz structure of SiO_2, but with the silicon atoms replaced alternately by aluminium and phosphorus atoms. The structural data are given in detail in [4–6]. Under ambient conditions, left- and right-handed $AlPO_4$ is described by the space groups $P3_121$ (D_3^4) and $P3_221$ (D_3^6), respectively. As structural units we have slightly deformed tetrahedra of different sizes linked by a common oxygen atom as shown in figure 1. The bond lengths within the two types of tetrahedra differ by about 10% and are collected in table 1. The tetrahedra are tilted with respect to the high-symmetric arrangement realized in the β-phase (space group $P6_222/P6_422$), the tilt angle providing an order parameter for the α–β transition. Corresponding to the sign of this order parameter two different species can be distinguished in the α-phase, well known as Dauphiné twins. Because of the alternating arrangement of AlO_4 and PO_4 tetrahedra the unit cell of $AlPO_4$ is doubled along the c-axis as compared with that of SiO_2 and, consequently, the Brillouin zone is halved. A sketch of the first Brillouin zone is shown in figure 2 along with the notations for the high-symmetry points and directions. There are 18 atoms (3 formula units) per primitive cell. Hence, 54 phonon branches are expected, twice as many as in quartz. These branches may be characterized by their symmetry properties.

Table 1. Interatomic next-neighbour distances in $AlPO_4$. All values are given in Å. The notation corresponds to figure 1.

Al–O_0	1.75
Al–O_1	1.73
Al–O_2	1.75
Al–O_3	1.73
P–O_0	1.51
P–O_4	1.52
P–O_5	1.51
P–O_6	1.52
O_0–O_1	2.83
O_0–O_2	2.90
O_0–O_3	2.80
O_0–O_4	2.47
O_0–O_5	2.49
O_0–O_6	2.46

According to the space group, six symmetry operations leave the lattice invariant: the identity (E), the 120° (D_{120}) rotation and the 240° (D_{240}) rotation, accompanied

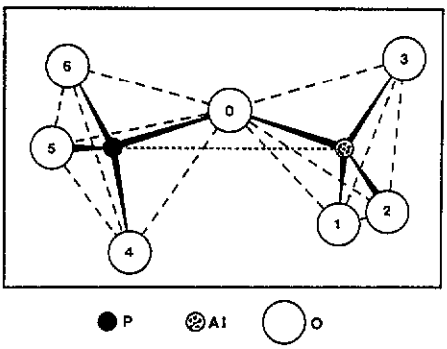

Figure 1. Definition of neighbouring atoms in the $AlPO_4$ structure: the notation for the different oxygen atoms, corresponding to table 1, is given along with a schematic representation of the uniaxial force constants marked by broken lines.

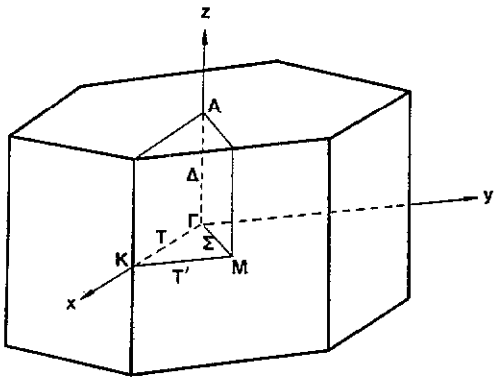

Figure 2. The Brillouin zone scheme in the hexagonal system.

by the fractional translation $c/3$, and the three 180° rotations D'_{180}, D''_{180}, D'''_{180} along the three equivalent [110] directions.

Conveniently, the phonon dispersion is displayed along the main symmetry directions T ([$\xi\xi$0]), Σ ([ξ00]) and Δ ([00ξ]) in reciprocal space connecting the Γ point with the zone-boundary points K, M and A, respectively (see figure 2). The line T' between K and M is another principal symmetry direction on the zone boundary. Group theory provides three irreducible representations Γ_1, Γ_2, Γ_3 at the Γ point which are

	Γ_1	Γ_2	Γ_3
E	1	1	$\begin{pmatrix} 1 & 0 \\ 0 & 1 \end{pmatrix}$
D_{120}	1	1	$\begin{pmatrix} \epsilon & 0 \\ 0 & \epsilon^* \end{pmatrix}$
D_{240}	1	1	$\begin{pmatrix} \epsilon^* & 0 \\ 0 & \epsilon \end{pmatrix}$
D'_{180}	1	−1	$\begin{pmatrix} 0 & 1 \\ 1 & 0 \end{pmatrix}$
D''_{180}	1	−1	$\begin{pmatrix} 0 & \epsilon \\ \epsilon^* & 0 \end{pmatrix}$
D'''_{180}	1	−1	$\begin{pmatrix} 0 & \epsilon^* \\ \epsilon & 0 \end{pmatrix}$

($\epsilon = e^{i2\pi/3}$, $\epsilon^* = e^{-i2\pi/3}$). The decomposition of the 54 phonons is

$$8\Gamma_1 + 10\Gamma_2 + 18\Gamma_3.$$

Acoustic modes belong to Γ_2 and Γ_3. The same irreducible representations apply for the K point (K_1, K_2, K_3).

Along T, however, the point group of the wavevector consists of the elements E and D'_{180}, only. Hence, there are two one-dimensional irreducible representations:

	T_1	T_2
E	1	1
D'_{180}	1	−1

An analogous table applies for the T' line and the M point. Along the Σ line group theory does not provide any decomposition of phonons. The group of wavevectors along the Δ line is cyclic and contains the symmetry elements E, D_{120} and D_{240}. The corresponding one-dimensional representations are

	Δ_1	Δ_2	Δ_3
E	1	1	1
D_{120}	1	ϵ	ϵ^*
D_{240}	1	ϵ^*	ϵ

At the zone boundary A along [00ξ], the symmetry group is the full point group and, hence, three multiplier representations are provided, one of which is two-dimensional:

	A_1	A_2	A_3
E	1	1	$\begin{pmatrix} 1 & 0 \\ 0 & 1 \end{pmatrix}$
D_{120}	ϵ	ϵ	$\begin{pmatrix} \epsilon^* & 0 \\ 0 & 1 \end{pmatrix}$
D_{240}	ϵ^*	ϵ^*	$\begin{pmatrix} \epsilon & 0 \\ 0 & 1 \end{pmatrix}$
D'_{180}	1	−1	$\begin{pmatrix} 0 & 1 \\ 1 & 0 \end{pmatrix}$
D''_{180}	ϵ	$-\epsilon$	$\begin{pmatrix} 0 & \epsilon^* \\ 1 & 0 \end{pmatrix}$
D'''_{180}	ϵ^*	$-\epsilon^*$	$\begin{pmatrix} 0 & \epsilon \\ 1 & 0 \end{pmatrix}$

The compatibility relations are shown in table 2 along with the decomposition of the 54 phonon branches.

These symmetry considerations are very useful in order to distinguish between the various branches and to interpret the experimental results described below.

Table 2. Compatibility relations for phonons along the main symmetry directions in $AlPO_4$.

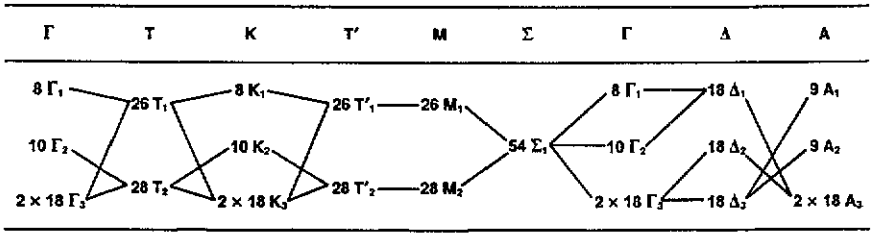

3. Experimental details

Inelastic neutron scattering experiments have been performed using the three-axis spectrometer UNIDAS for thermal neutrons at the FRJ-2 reactor of the KFA Jülich. Pyrolytic graphite crystals were used as the double monochromator and analyser. Usually, a scan mode with a fixed incident neutron energy of 14.77 meV ($k_i = 2.665$ Å^{-1}) was used. Higher-order contamination was reduced by a graphite filter. The spectrometer resolution was optimized according to the energy range of the measured excitations using collimations between 0.15° and 0.75°. For reasons of intensity and resolution we restricted ourselves to the low-frequency part (< 8 THz) of the phonon dispersion. The simultaneous use of an Eulerian cradle, on the one hand, and of model calculations yielding phonon intensities, on the other hand, enabled us to select the most appropriate Brillouin zones for the detection of individual phonons. This technique was especially useful and its use was sometimes inevitable in order to assign observed phonons to the correct branches. Details of the calculations are described below.

The $AlPO_4$ sample was grown by D F Croxall (General Electric Company, Hirst Research Centre, Wembley, Middlesex, UK) under hydrothermal conditions. The single crystal of rhombohedral habit exhibited high optical quality and a volume of about 3 cm^3.

4. Results

The low-energy part of the phonon dispersion for $AlPO_4$ at room temperature is displayed in figure 3. The points represent experimental data, whereas the lines show the results of lattice dynamical model calculations described below. For a hexagonal lattice it is convenient to draw phonon branches along a closed loop of wavevectors within the basal plane (cf figure 2): leaving the zone centre in the direction $[\xi 00]$ (Σ), the zone boundary is reached at the M point; direction $[-\xi\, 2\xi\, 0]$ (T') on the zone boundary leads from M to K; finally, along $[\xi\xi 0]$ (T) the Γ point is approached. In figure 3, phonons of different symmetries along T and T' are displayed in separate diagrams. Along $[\xi 00]$ all phonons belong to the same irreducible representation. For clarity, these branches are drawn twice (first and fourth section of figure 3) in order to illustrate the compatibility relations at the M point. Having in mind the transition to the incommensurate phase that occurs in the x–y plane, we placed emphasis on the Σ and T lines. For phonon wavevectors along the Δ line only two branches are measured. Therefore, the three representations Δ_1, Δ_2 and Δ_3 are superimposed

within the same diagram and distinguished by different types of line. Experimental phonon frequencies for selected wavevectors along the principal symmetry directions are listed in table 3.

The density of phonon branches is much larger in $AlPO_4$ than in quartz. Hence, there is a variety of 'crossover' effects, especially along Σ. In the energy region investigated fourteen external lattice modes are found in addition to the three acoustic branches. For comparison, in quartz the same frequency region covers only three optical and the acoustic modes. Frequently, the identification of phonons with similar energies was possible only with the help of phonon intensity calculations.

Table 3. Phonon frequencies of α-$AlPO_4$. In the left-hand column, the directions in the Brillouin zone are indicated. Along $[\xi\xi 0]$ the data are arranged according to the two irreducible multiplier representations, just as in figure 2. The second column gives the wavevectors in reciprocal-lattice units.

ξ		phonon frequencies in THz							
Γ		1.5	3.3	3.8	4.7	4.9	6.0		
$[\xi 00]$ Σ	0.1	0.8	1.2	3.4	3.8	5.5			
	0.2	1.35	2.2	3.5	4.0	5.2	6.15		
	0.3	1.65		4.4	5.5	6.2	6.8		
	0.4	1.8	3.0	3.5	3.7	4.2	6.2	7.5	
M		1.85	1.95	2.15	3.0	3.6	4.4	6.3	8.2
$[\xi\xi 0]$ Γ_1 / Γ'_1	0.1	1.7		3.8	5.0	5.8			
	0.2	2.7	2.9	4.5	4.9				
	0.3	2.5	3.1	6.4					
	0.4	2.35	3.5	4.7					
$[\xi\xi 0]$ Γ_2 / Γ'_2	0.1	1.2	2.2	3.3	3.6	4.3	5.8		
	0.2	2.1	2.15	2.9	3.8	6.1			
	0.3	2.05	2.3	3.9					
	0.4	2.0	2.3	2.9	3.5	4.7			
$[00\xi]$ Λ	0.1	1.5							
	0.2	0.65	1.45						
	0.3	1.0	1.45						
	0.4	1.35							
A		1.3	2.15						

At first sight, it appears surprising that in $AlPO_4$ the first optical Γ-point mode ($\simeq$ 1.5 THz) exhibits a much lower frequency than in quartz. In fact, this mode is a result of the doubling of the unit cell and corresponds to the transverse acoustic mode at the zone boundary in quartz (the A point). A direct comparison of quartz and $AlPO_4$ phonons can be made with the help of figure 4: along $[00\xi]$ the dispersion of the lowest-frequency branches for $AlPO_4$ can be obtained nearly quantitatively

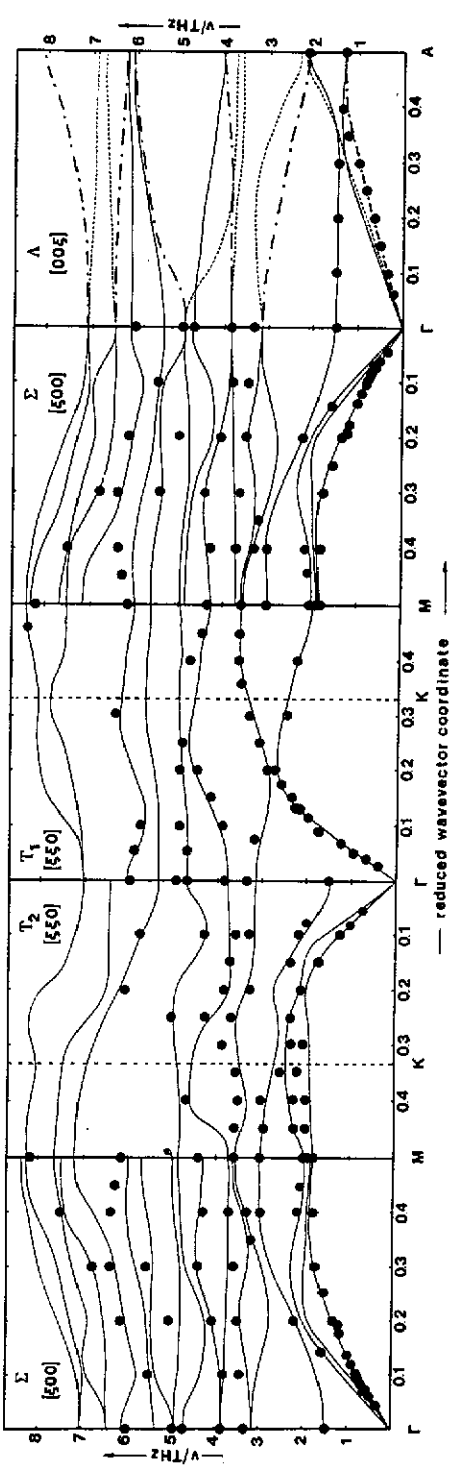

Figure 3. Phonon dispersion of α-$AlPO_4$ along the principal symmetry directions: T_1 and T_2 denote the two different irreducible representations along [ξξ0]. For compatibility reasons the dispersion along [ξ00] is drawn twice. In direction [00ξ] modes of different symmetries are distinguished by different types of line (Δ_1; ——; Δ_2; — · —; Δ_3; – – –). The points are experimental results, while the curves are calculated from lattice dynamical model 1 described in the text.

from the quartz data of [7] just by folding the branches at $\pi/2c_{SiO_2}$. This is not only true for the Γ-point modes but even for the whole Δ direction confirming the great similarity of the two compounds as regards their dynamics. In 1960 Scott [8] had already predicted the 1.5 THz mode on the basis of his Raman data. As this mode is not Raman active, however, it was observed for the first time in our neutron scattering study [9, 10]†.

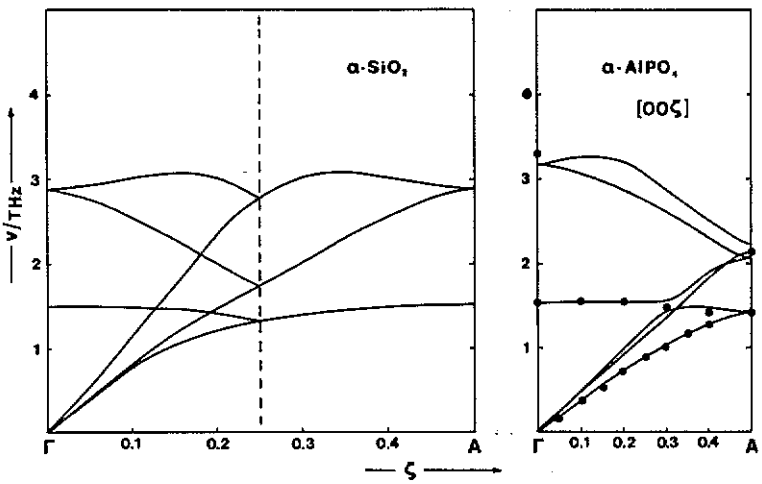

Figure 4. Comparison of Δ phonons in quartz and $AlPO_4$: the phonon dispersion of $AlPO_4$ is obtained by back-folding the dispersion of quartz at the wavevector $q = 0.25a^*$. The points are experimental results from the present work. The phonon dispersion of quartz in the Δ direction is taken from [7].

Disregarding phonon interactions, it is surprising that the replacement of silicon by aluminium and phosphorus hardly influences the dynamics of the quartz structure. Even quantitatively, there is only a small overall shift of external phonon frequencies to lower values in $AlPO_4$. As an example, the longitudinal acoustic (LA) mode along [ξξ0] is considered. Its zone-boundary frequency in quartz is about 4 THz [12] as compared with 3.5 THz in $AlPO_4$. Note that, due to eigenvector exchange with the lowest total-symmetrical optical mode (the T_1 representation) in $AlPO_4$ at $\xi \simeq 0.2$, it is, in fact, the second branch of this representation near the K point that carries the characteristics of the LA phonon.

In quartz, an anomaly of sound velocities in direction Γ–K was detected by Dorner *et al* [12]. At small wavevectors, these authors found the LA branch just in between the two transverse ones. The corresponding modes in $AlPO_4$ have been measured very carefully. In contrast to what was observed in SiO_2, however, no anomaly could be found.

5. Model calculations and discussion

Model calculations for the phonon dispersion in $AlPO_4$ have been performed using the program package UNISOFT [13, 14]. This program allows one to specify each

† Quite recently, this mode has also been detected by infrared spectroscopy at 10 K [11].

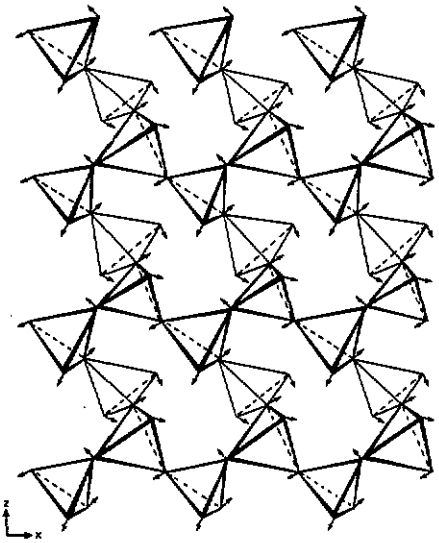

Figure 5. Representation of eigenvectors of the soft mode at the Γ point: in this figure only the tetrahedra of the $AlPO_4$ structure are shown. The eigenvectors are indicated by small arrows.

individual pair interaction, which can be selected from different model potentials. Phonon frequences $\nu_{q\zeta}$ ($\zeta = 1, \ldots, 3N$, N = number of atoms within the primitive cell) for arbitrary points q within the Brillouin zone are calculated along with their respective eigenvectors $e_\kappa(\zeta|q)$ ($\kappa = 1, \ldots, N$). The vibrations are automatically arranged according to their symmetry (the irreducible multiplier representation). The phonon intensities $|F_{q\zeta}(g)|^2$, as measured in inelastic neutron scattering experiments (dynamical structure factors), are calculated for arbitrary Brillouin zones g:

$$F_{q\zeta}(g) = \sqrt{\frac{\hbar}{2M_\kappa}} \sum_\kappa b_\kappa \exp(-W_{j\kappa}(g+q)) \exp(\mathrm{i}(g+q)R_\kappa)(g+q)e_\kappa(\zeta|q) \quad (5.1)$$

(M_κ, b_κ, W_κ, R_κ being the mass, coherent scattering length, Debye–Waller exponent and position vector of atom κ, respectively). Thus, this program package was especially useful in enabling us to label the experimentally determined phonons and to detect those modes that exhibit a sufficiently large structure factor only in general Brillouin zones where predictions cannot be made by simple arguments. Symmetry provides some general extinction rules for momentum transfers $g + q$ along special directions: For $g \| q \| [\xi\xi 0]$ only phonons of the symmetric representation T_1 (T_1') are visible; for $g \| q \| [00\xi]$ the representations Δ_1, Δ_2, Δ_3 are only active for $g = 3nc^*$, $g = (3n+1)c^*$, $g = (3n+2)c^*$, respectively.

Starting from Barron's model for quartz [15] we have examined different extensions. The following four models can be distinguished.

(1) A force constant model with first- and second-neighbour interaction only and no distinction between interactions within the tetrahedra.

(2) Model 1, but taking into account the differences between AlO_4 and PO_4 tetrahedra.

(3) An extension of model 2 to more than nearest neighbours (interactions up to 7 Å were taken into account).

(4) A modified rigid-ion model (covalent bonds were simulated by longitudinal and transverse springs).

In order to fulfil stability criteria we always took care to satisfy the condition of rotational invariance.

The model calculations have been performed for wavevectors along the principal symmetry directions $[\xi 00]$, $[\xi\xi 0]$ and $[00\xi]$. The lines in figure 3 are the results from using model 1 where the longitudinal (L) and transverse (T) force constants

$$L = \mathrm{d}^2 V(\kappa l, \kappa' l')/\mathrm{d}r^2|_{r=|r^0_{\kappa' l'} - r^0_{\kappa l}|} \tag{5.2}$$

$$T = (1/r)\,\mathrm{d}V(\kappa l, \kappa' l')/\mathrm{d}r|_{r=|r^0_{\kappa' l'} - r^0_{\kappa l}|} \tag{5.3}$$

were used as model parameters. The following interactions have been taken into account:

(i) aluminium (phosphorus)–oxygens 0, 1, 2, 3 (intra-tetrahedral interaction);
(ii) aluminium–phosphorus (inter-tetrahedral interaction); and
(iii) oxygen–oxygen (first- and second-nearest neighbours)(framework interaction),

according to the scheme shown in figure 1.

Obviously, the agreement between calculation and experiment is surprisingly good even for this extremely simple model which requires only five independent parameters! The final parameter values are listed in table 4. Note that the transverse force constants $T_{\mathrm{Al-O}}$ ($T_{\mathrm{P-O}}$) and $T_{\mathrm{O-O}}$ are not independent. Instead, the conditions of rotational invariance give rise to the constraint

$$T_{\mathrm{Al-O}} = -4T_{\mathrm{O-O}}. \tag{5.4}$$

For comparison the corresponding quartz parameters of [15] are also included in this table. The differences between the two parameter sets are quite small even though the bond lengths (table 1) and the atomic radii differ significantly. In particular, the transverse force constants are nearly identical.

Table 4. Values of force constants for $AlPO_4$. The parameters are evaluated using the force constant model described in the text. All values are given in N m^{-1}. L and T denote the longitudinal and transverse force constants in a central-force model. O′ denotes next-nearest neighbours up to 3.65 Å. The parameters for quartz [15] are given in parentheses.

	L	T
Al, P–O	450(413)	56(51.5)
O–O	30(42.1)	−14(−12.3)
O–O′	1.3	0
Al–P	50(77.8)	0(2.2)

Table 5 shows a comparison between the calculated Γ-point frequencies and Raman, infrared and neutron frequencies. The Γ_1 representation is only Raman active, the Γ_2 representation is only infrared active and the twofold-degenerate Γ_3 representation is both Raman and infrared active. The agreement between the calculated and the experimentally determined phonon frequencies is unexpectedly good

Table 5. Raman, infrared and neutron Γ-point modes compared with calculated modes (force constant model). All frequencies are given in THz. Raman data are taken from [8] and infrared data from [11]. The double values in some IR data are for different samples.

IMR	ν_{calc}	ν_{Raman}	$\nu_{infrared}$	$\nu_{neutron}$
	5.59			
	6.13	6.5		
	10.0	10.1		
Γ_1	10.56	-		
	12.85	13.7		
	23.39	21.9		
	31.23	33.2		
	33.51	33.50		
	1.44		1.43	1.5
	4.71		4.19	4.7
	10.21		8.08/11.22	
Γ_2	10.90		13.17	
	14.22		14.67/15.41	
	23.11		20.47	
	23.24		-	
	33.86		32.78	
	33.93		34.73	
	3.19	3.14	3.35	3.3
	3.87	3.51	3.77	3.8
	4.85	4.7?	4.94	4.9
	6.54	5.81	5.92	6.0
	7.06	-	-	
	9.82	8.86	8.53	
	11.44	11.11	11.34	
	13.34	12.49	12.39	
Γ_3	13.39	13.77	14.16	
	16.16	17.01	-	
	20.52	20.87	19.46	
	22.96	21.35	21.25	
	23.22	-	22.09	
	32.21	-	32.93	
	33.54	-	33.83	
	33.58	33.83	35.32	
	33.90	36.85	36.77	

over the whole energy range. Even the energy gap between the 'internal' modes and the 'lattice' modes in the range 23 to 32 THz is represented very well.

The extended models 2–4, despite requiring many more (up to 18) independent parameters, did not improve the fit significantly. Hence, the essential features of the phonon dispersion are found to be already represented by just the few data of table 4. In particular, the difference between aluminium and phosphorus enters into the lattice dynamics of $AlPO_4$ merely via their masses. Further interactions need not be taken into account, at least if one is only concerned with the low-frequency phonons. We therefore refrain from presenting detailed results for the extended force

constant models 2 and 3.

In model 4, in addition to inter-tetrahedral and framework interactions, we have taken into account Coulomb interactions. The effective charges have been determined to $0.6e$ for aluminium, $0.8e$ for phosphorus and $-0.35e$ for oxygen. As already suggested by Scott [8], these charges differ strongly from the formal charges. Furthermore, the difference between the charges of the inter-tetrahedral atoms seems not to be significant. This behaviour indicates an effective screening of charges by the oxygen framework, which may be why the extremely simple Born–von Karman model, model 1, describes the principal features of the $AlPO_4$ phonon dispersion quite well. Thus, it is the oxygen framework that determines the low-frequency part of the phonon dispersion rather than the central atoms.

Apart from the absolute values, it is most interesting to study the influence of different force constants upon the details of the phonon dispersion. High-energy modes are adjusted by the longitudinal intra-tetrahedral interactions (Al, P)–O. They are fitted to Raman and infrared modes (table 5). The main effect of O–O force constants is observed in the medium-energy region between 3 THz and 20 THz where the influence of the longitudinal modes is especially pronounced at larger wavevectors. Moreover, zone-boundary modes are sensitive to changes of the longitudinal Al–P (inter-tetrahedral) force constants. The second-nearest-neighbour interactions are needed in order to stabilize the low-energy modes within the Brillouin zone.

Because of the large density of phonon dispersion branches in direction $[\xi 00]$, the agreement between observed phonon spectra and the results of model calculations (figure 3) in the energy region above 5 THz could be regarded as being accidental. This is, however, not the case. Instead, the assignment of measured phonons to distinct branches was achieved by comparing not only frequencies but also intensities. Moreover, some phonons could only be found experimentally after we had calculated the inelastic structure factors (equation (5.1)) which served as a guide for selecting the most appropriate Brillouin zone.

Within the frequency range between 5 and 8 THz, e.g., there are as many as six branches that exchange their respective eigenvectors. Hence, there is a particular Brillouin zone (220) in which the relative intensities of these six phonons vary strongly as a function of phonon wavevector. Phonons measured in this zone thus belong to different branches. At the Γ point (220) the doubly degenerate mode at 4.9 THz is visible, whereas at M (2.5 2 0) the upper mode at 8.2 THz is observed. On the other hand, in the Brillouin zone (310) phonons with eigenvectors corresponding to a transition between the two Dauphiné twins are observed (figure 5). The frequency of these phonons hardly depends on the wavevector. At Γ we found 6.0 THz and at M we obtained 6.3 THz. Again, these phonons belong to different branches due to eigenvector exchange. It should be noted that these phonons soften dramatically on approaching the phase transition at about 847 K. Here, anharmonic effects may be expected. Hence, it is not surprising that the agreement between experiment and our simple model calculations is less perfect for this mode near the zone boundary as compared with the overall fit. Consequently, these shortcomings are not even reduced by the other models described above.

In direction $[\xi\xi 0]$ the agreement between experimental spectra and lattice dynamical calculations for the total symmetric irreducible representation is extremely good. Here, the 6 THz tilt mode is clearly separated from the neighbouring branches of the same symmetry and exhibits almost no dispersion. The eigenvector exchange of the longitudinal acoustic branch and the first optical mode at $q = 0.2a^*$ is re-

produced very well. At the 'crossover' point there is almost no energy gap between the two modes. This also applies to the third and the fourth mode of the same representation. Hybridization and anticrossing effects are thus completely described within the harmonic approximation.

As for the antisymmetric representation in direction [$\xi\xi$0], again a good number of 'mixed' eigenvector states are observed below 5 THz, in excellent agreement with the calculations. This finding is consistent with the assumption that it is those modes that exhibit the lowest frequencies that leave the AlO_4 and PO_4 tetrahedra essentially undistorted. Modes of this kind, however, do not have a simple eigenvector like purely acoustic ones. Hence, the lowest-frequency zone-boundary modes never show an eigenvector of the acoustic type.

Just as in quartz [9, 1], the tilt mode near 6 THz with eigenvectors corresponding to the transition between Dauphiné twins (figure 5) is strongly temperature dependent. Its softening is related to structural properties rather than to a change of effective interatomic force constants: on heating, the static distortion of the lattice, as represented by the twin angle, decreases and vanishes at the phase transition to the high-symmetry β-phase at 847 K. Thus, the structure changes continuously with temperature. If the present lattice dynamical model, with the parameters listed in table 1, is applied to structures at different temperatures, the softening of the tilt mode can easily be reproduced, at least qualitatively. Other modes are less affected. There is no need for changing parameter values. Obviously, the dynamics is very well represented by our model and the frequency shift of the tilt mode is simply caused by the temperature dependence of the static lattice distortion, i.e. the order parameter for the α–β transition.

In quartz, it could be shown that the interaction of this mode with the TA phonon corresponding to the elastic constant c_{66} is responsible for the formation of the incommensurate phase [1]. In $AlPO_4$, however—and this is one of the differences from the case of quartz—the coupling mechanism of this soft mode may be more complicated due to the additional low-lying branches within the smaller Brillouin zone. Along both the Δ direction and the Σ direction, the soft mode and the 1.5 THz mode, e.g., belong to the same irreducible representation and can therefore interact. This is true for not only the α-phase but also the β-phase. A detailed discussion of the dynamical behaviour of $AlPO_4$ near the incommensurate phase will be given in a subsequent paper.

6. Conclusion

The low-frequency part (< 8 THz) of the phonon dispersion of α-$AlPO_4$ has been measured by inelastic neutron scattering. The experimental data are compared with different lattice dynamical models. The essential lattice dynamical features can be reproduced by even a very simple Born–von Karman model, represented by five independent parameters only. Long-range forces do not play a significant role and, in particular, Coulomb forces seem to be effectively screened by the oxygen framework. Moreover, there is only very little difference between Al and P interactions. The low-frequency phonon dispersion is obviously governed by the oxygen framework rather than the central atoms. On this basis the great similarity between quartz and $AlPO_4$ as regards not only the lattice dynamics but also the transformation behaviour seems reasonable. Having in mind, however, that the incommensurate

phase in quartz is a result of phonon coupling processes, the situation in $AlPO_4$ turns out to be more complicated because of the larger density of phonon branches. A detailed experimental investigation of the high-temperature dynamics and transition mechanisms to the incommensurate phase will be presented in a subsequent paper.

Acknowledgments

The high-quality $AlPO_4$ single crystal used for the present study was kindly supplied by D F Croxall. Fruitful discussions with H Arnold are gratefully acknowledged. This work was funded by the German Federal Minister for Research and Technology (BMFT) under contract number 03-HA1AAC-6.

References

[1] Bethke J, Dolino G, Eckold G, Berge B, Vallade M, Zeyen C M E, Hahn T, Arnold H and Moussa F 1987 *Europhys. Lett.* 3 207
[2] Arnold H, Bethke J, Eckold G, Hahn T and Min-Hua J 1984 *Acta Crystallogr. Suppl.* A 40 C-134
[3] Chang Y P and Barsch G R 1976 *IEEE Trans. Son. Ultrason.* 23 127
[4] Schwarzenbach D 1966 *Z. Kristallogr.* 123 161
[5] Ng H N and Calvo C 1976 *Can. J. Phys.* 54 638
[6] Bethke J 1982 *Diplomarbeit* RWTH Aachen
[7] Elcombe M M 1967 *Proc. Phys. Soc.* 91 947
[8] Scott J F 1971 *Phys. Rev.* B 4 1360
[9] Bethke J 1988 *KFA Jülich Report* JÜL-2185
[10] Arnold H, Bethke J, Eckold G and Hahn T 1984 *HMI Berlin Report* HMI-B 411 p 180
[11] Camassel J, Goullet A and Pascual J 1988 *Phys. Rev.* B 38 8419
[12] Dorner B, Grimm H and Rzany H 1980 *J. Phys. C: Solid State Phys.* 13 6607
[13] Eckold G, Stein-Arsic M and Weber H-J 1986 *KFA Jülich Report* JÜL-Spez.-366
[14] Eckold G and Stein-Arsic M 1987 *J. Appl. Crystallogr.* 20 134
[15] Barron T H K, Huang C C and Pasternak A 1976 *J. Phys. C: Solid State Phys.* 9 3925